DTU Library

Design of composite structures with programmable elastic responses under finite deformations

Li, Weichen; Wang, Fengwen; Sigmund, Ole; Shelly Zhang, Xiaojia

Design of composite structures with programmable elastic responses under finite deformations

Weichen Li[a], Fengwen Wang[b], Ole Sigmund[b], Xiaojia Shelly Zhang[a,c,*]

[a]*Department of Civil and Environmental Engineering, University of Illinois Urbana-Champaign, 205 North Mathews Ave, Urbana, IL 61801, USA*
[b]*Department of Mechanical Engineering, Technical University of Denmark, Nils Koppels Alle, Building 404, 2800 Kongens Lyngby, Denmark*
[c]*Department of Mechanical Science and Engineering, University of Illinois Urbana-Champaign*

Abstract

We systematically design composite structures using multi-material topology optimization to achieve tunable elastic responses under finite deformations. We formulate an inverse problem where the errors between the actual (numerical) and the prescribed force-displacement curves are minimized. The framework harnesses multiple hyperelastic materials with distinct constitutive relations, which enlarge the design space of programmable structures compared to the single-material setting. A stress constraint for multi-material structures is proposed to control the levels of stress and deformation in the optimized composite structures with distinct stress limits. Through several numerical design scenarios, we design multi-material structures that achieve a variety of programmed load-displacement curves, some of which are physically unattainable with single materials. The optimized structures exhibit unconventional geometries and multi-material distributions and reveal distinct mechanisms, such as converting deformation modes from flexure-dominated to stretch-dominated. Multiple designs achieving the same target response are identified, demonstrating the effectiveness of the proposed methodology to explore various composite structures with programmable responses.

Keywords: Programmable structures, force-displacement relations, topology optimization, multi-material, finite deformation, stress constraint

1. Introduction

Novel material and structural systems with programmable properties are highly desirable in various engineering applications. A vast amount of studies have devoted to realize those systems with various unconventional properties, such as negative Poisson ratios [1, 2], prescribed stress-strain relations [3, 4],
5   enhanced energy trapping and absorption capabilities [5, 6], tunable material elastic properties [7, 8], and tunable deformation [9]. Among the various properties, this work focuses on designing structures with programmable force-displacement responses, which has many important applications such as programming the touch response of physical buttons [10], patterning cell alignments with soft materials [11], and designing strong-action soft robots [12, 13].
10   As a powerful computational design methodology, topology optimization has demonstrated its great potential in designing novel materials and structures with unique behaviors. At the material level, topology

---

*Corresponding author
Email address: zhangxs@illinois.edu (Xiaojia Shelly Zhang)

optimization has been adopted in many studies to design novel microstructures with engineered properties, such as negative Poisson's ratio [1, 2], negative thermal expansion coefficient [14], tunable elastic modulus [7, 8] and stress-strain relations [1, 2], photonic and phononic bandgap [15, 16], and improved piezoelec-
15 tric properties [17]. At the structure level, topology optimization has been adopted to program unconventional force-displacement responses, including programming the snap-through [18] and hardening/softening responses of slender structures [19] and controlling the force-displacement path of compliant mechanisms [20].

Composite materials and structures possess many attractive properties that are unavailable in single-material ones. Recent advances in both manufacturing and design make the realization of novel composites
20 with programmable behaviors possible. On the manufacturing side, advances in multi-material additive manufacturing (AM) technologies allow for the fabrication of composites with complex geometries and material distributions [21]. From the design perspective, multi-material topology optimization has gained growing interests and has been applied to, e.g., designing engineering structures [22] and composites with tunable thermal expansions [23] and auxetic behaviors [24]. Comparing to single-material topology optimization, the
25 consideration of multiple candidate materials with distinct properties in the multi-material topology optimization greatly enlarges the design space and, thus offers more freedom and flexibility to achieve a wider range of programmable behaviors.
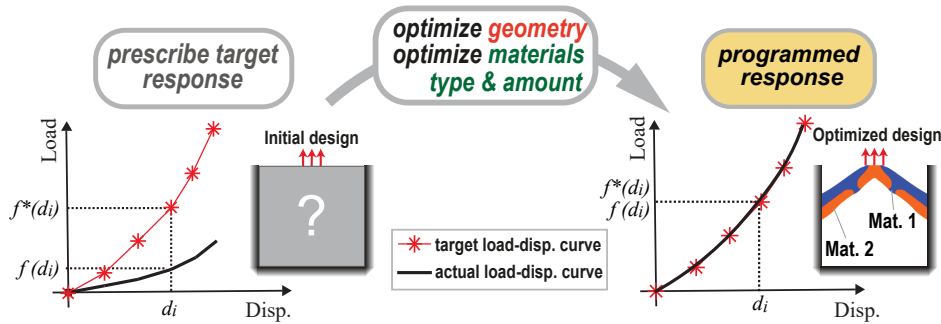

Figure 1: Illustration of the overall goal of this work. The goal is to optimize geometry, material types, and material distributions to achieve the prescribed load-displacement curve. At a control point d_i, $f^*(d_i)$ and $f(d_i)$ are the prescribed force and actual force.

In this study, we systematically design composite structures through a multi-material topology optimization methodology to achieve a wide range of programmed force-displacement relations under finite deforma-
30 tions. The overall goal of the proposed methodology, as illustrated in Figure 1, is to minimize the maximum norm of errors between the actual and prescribed load-displacement curves on a set of control points. Given a problem setup with an initial design, the proposed approach not only optimizes the structural geometry but also selects the types and amount of different materials, so that the actual force-displacement response of the optimized design achieves the prescribed target response. Existing multi-material topology optimization
35 formulations in the literature, consider either multiple linear materials or nonlinear materials (described by the same stored energy function) with different Young's moduli, which cannot effectively interpolate nonlinear and deformation-dependent response of multiple soft materials and severely limits the range of programmable responses. The proposed formulation accounts for two (can be directly generalized to any number) hyperelastic materials characterized by distinct stored energy functions and nonlinear elastic behaviors (e.g., hardening
40 and softening) as well as a void phase. To address the excessive distortion and numerical instability of low-density (void) elements in topology optimization under large deformations [1, 25], the energy interpolation approach based on a linear modeling of the void regions [1, 25] is adopted and shown to be effective in

the design examples. Another challenge is to effectively prevent the potential appearance of thin members and unrealistically large deformation concentration in the multi-material optimized structures. To address this challenge, we propose a novel stress constraint formulation that simultaneously accounts for both the distinct nonlinear elastic behaviors and stress limits of different candidate materials. Through several design scenarios, we discover unconventional composite structures with force-displacement responses and reveal the underlying mechanisms under large deformations, including a linear one (achieved by mixing highly nonlinear materials), and a mechanism-like one with an acute stiffening region. We also show that considering two materials can realize certain force-displacement relations that are physically unattainable with either of the two.

The remainder of the paper is organized as follows. Section 2 briefly reviews the hyperelastic material model used and the nonlinear finite element method (FEM). Section 3 presents the design parameterization of composite structures and formulates the multi-material topology optimization framework. Section 3 also introduces a stress constraint function that accounts for both distinct nonlinear elastic behaviors and stress limits of different candidate materials. In section 4, we present several numerical experiments considering three design scenarios with different target load-displacement relations, and discuss the design, performance, and implications of the obtained structures. Section 5 contains several concluding remarks. An appendix complements the paper, which presents an alternative formulation and corresponding designs with programmed responses.

2. Hyperelastic constitutive models and nonlinear finite element approximation

This section reviews the hyperelastic material model and the nonlinear FEM for finite elasticity, which forms the basis of this study. The behavior of an isotropic, inhomogeneous hyperelastic solid can be characterized by a stored energy function $W\left(\boldsymbol{x}, \lambda_1, \lambda_2, \lambda_3\right)$, where $\boldsymbol{x}$ is the position vector in the reference configuration, and λ_a, $a = 1, 2, 3$ are the principal stretches of the right Cauchy-Green deformation tensor $\boldsymbol{C} = \boldsymbol{F}^T \boldsymbol{F}$ with $\boldsymbol{F} = \boldsymbol{I} + \nabla \boldsymbol{U}$ being the deformation gradient tensor and $\boldsymbol{U}$ being the displacement vector. We adopt the second Piola-Kirchhoff (2nd PK) stress measure, which is expressed in spectral form as

$$\boldsymbol{S} = \sum_{a=1}^{3} \frac{1}{\lambda_a} \frac{\partial W}{\partial \lambda_a} \boldsymbol{M}^{(a)} \otimes \boldsymbol{M}^{(a)}, \tag{1}$$

where $\boldsymbol{M}^{(a)}$ is a unit vector pointing to the principal direction of $\boldsymbol{C}$ associated with λ_a.

Various hyperelastic material models are available with different expressions of W. This work adopts a compressible Ogden model [26, 27] for its generality and flexibility in controlling the level of nonlinearity and tension-compression asymmetry of the stress-strain relations. The stored energy function of the adopted Ogden model is

$$W\left(\lambda_1, \lambda_2, \lambda_3\right) = \sum_{a=1}^{M} \left[\frac{\mu_a}{\alpha_a} \left(\lambda_1^{\alpha_a} + \lambda_2^{\alpha_a} + \lambda_3^{\alpha_a} - 3 \right) \right] + \sum_{a=1}^{M} \frac{\mu_a}{\alpha_a \beta_a} (J^{-\alpha_a \beta_a} - 1), \tag{2}$$

where μ_a, α_a, and β_a are material parameters, M is the number of terms, and $J \doteq \det \boldsymbol{F}$. The initial shear modulus G and bulk modulus κ are given as $G = \frac{1}{2} \sum_{a=1}^{M} \mu_a \alpha_a$ and $\kappa = \sum_{a=1}^{M} \mu_a \alpha_a \left(\frac{1}{3} + \beta_a \right)$.

In this work, we focus on two-dimensional structures and assume a plane stress condition with $M = 1$ and drop the subscript a in subsequent expressions for conciseness. According to the following states of $\boldsymbol{C}$

3

and $\boldsymbol{S}$ in this condition (expressed in indicial notation): 1) $C_{i3} = C_{3i} = 0$, $i = 1, 2$, and $C_{33} \neq 0$ [28]; and 2) $S_{33} = \frac{1}{\lambda_3} \frac{\partial W}{\partial \lambda_3} = 0$; we obtain the expression of λ_3 in terms of λ_1 and λ_2 as

$$\lambda_3 \left(\lambda_1, \lambda_2\right) = \left(\lambda_1 \lambda_2\right)^{-\beta/(\beta+1)}. \tag{3}$$

Substituting (3) into (2) gives the stored energy function of the Ogden model under the plane stress condition, $\hat{W}\left(\lambda_1, \lambda_2\right) = W\left(\lambda_1, \lambda_2, \lambda_3(\lambda_1, \lambda_2)\right)$, based on which the stress-stretch relation can be obtained. We note that the plane stress condition allows for modeling near-incompressible behaviors (as in most elastomers) using standard FEM without locking.

We adopt the standard displacement-based formulation with a total Lagrangian approach [28]. Given a mesh of the domain discretized by the bi-linear quadrilateral finite elements, the total potential energy of the discrete system is given by:

$$\Pi\left(\boldsymbol{u}\right) = \sum_e \int_{\Omega_e} W\left(\boldsymbol{u}_e\right) \mathrm{d}\boldsymbol{x} - \left(\boldsymbol{f}^{ext}\right)^T \boldsymbol{u}, \tag{4}$$

where $\boldsymbol{u}$ is the displacement vector, $\boldsymbol{f}^{ext}$ is the external force vector. Equilibrium is given by the stationary condition of the total potential energy

$$\boldsymbol{r}(\boldsymbol{u}) = \frac{\partial \Pi}{\partial \boldsymbol{u}}\left(\boldsymbol{u}\right) = \boldsymbol{f}^{int}\left(\boldsymbol{u}\right) - \boldsymbol{f}^{ext} = \boldsymbol{0}, \tag{5}$$

where $\boldsymbol{r}(\boldsymbol{u})$ is the residual vector, and $\boldsymbol{f}^{int}(\boldsymbol{u})$ is the internal nodal force vector. Detailed expressions and implementation procedures can be found in [28]. The nonlinear equation (5) is solved using the Newton's method with inexact line search [29, 30]. In this study, all numerical examples consider displacement loading.

3. Multi-material topology optimization formulation

This section introduces the multi-material design parameterization and optimization formulation to design composite structures with programmable nonlinear elastic responses. The density-based topology optimization approach [31] is adopted.

3.1. Design parameterizations of composite structures

The overall design parameterization consists of two major components: 1) representing multi-material structures with several design and physical variables and 2) interpolating the stored energy function, stress tensor, and stress limits of the multi-material structures. This subsection describes these components in detail.

3.1.1. Representing multi-material structures

Design optimization of a composite consisting of two material phases (Material 1 and Material 2) requires the parameterizations of both topology and material phase distributions [32, 33]. The topology parameterization characterizes the spatial occupancy of material, i.e., whether a location in space is solid or void, and is associated with the density design variables, denoted by $\boldsymbol{\rho}$, with ρ_e for element e. The material parameterization describes the material types at each location in the design and is associated with the material design variables, denoted by $\boldsymbol{\xi}$, with ξ_e for element e. To regularize the design space and enhance the design discreteness, we employ the Heaviside projection [34] to both sets of design variables to obtain the physical

density and material variables, which are used to represent composite structures. The physical variables are computed by

$$\bar{\rho}_e = \frac{\tanh(\beta_\rho \eta_\rho) + \tanh\left(\beta_\rho\left(\tilde{\rho}_e - \eta_\rho\right)\right)}{\tanh(\beta_\rho \eta_\rho) + \tanh(\beta_\rho(1 - \eta_\rho))} \quad \text{and} \quad \bar{\xi}_e = \frac{\tanh(\beta_\xi \eta_\xi) + \tanh(\beta_\xi(\tilde{\xi}_e - \eta_\xi))}{\tanh(\beta_\xi \eta_\xi) + \tanh(\beta_\xi(1 - \eta_\xi))}, \tag{6}$$

where β_ρ and β_ξ are parameters controlling the discreteness of the projection, η_ρ and η_ξ are projection thresholds, and $\tilde{\rho}_e$ and $\tilde{\xi}_e$ are filtered variables defined as

$$\tilde{\rho}_e = \frac{\sum_{j \in Ne(R_\rho)} w\left(\boldsymbol{x}_j\right) v_j \rho_j}{\sum_{j \in Ne(R_\rho)} w\left(\boldsymbol{x}_j\right) v_j} \quad \text{and} \quad \tilde{\xi}_e = \frac{\sum_{j \in Ne(R_\xi)} w\left(\boldsymbol{x}_j\right) v_j \xi_j}{\sum_{j \in Nee(R_\xi)} w\left(\boldsymbol{x}_j\right) v_j}, \tag{7}$$

where $\boldsymbol{x}_j$ is the location of the centroid of element j, v_j is the corresponding element volume, N_e is the neighborhood of element e defined by a filter radius R, i.e. $N_e(R) = \{j : \|\boldsymbol{x}_j - \boldsymbol{x}_e\| \leq R\}$, $w\left(\boldsymbol{x}_j\right)$ is the linear weight function defined as $w\left(\boldsymbol{x}_j\right) = R - \|\boldsymbol{x}_j - \boldsymbol{x}_e\|$, and R_ρ and R_ξ are filter radii for ρ_e and ξ_e, respectively.

By construction, the physical density variable $\bar{\rho}_e$ parametrizes the topology of the design with $\bar{\rho}_e = 1$ and $\bar{\rho}_e = 0$ representing solid and void, respectively. The physical material variable $\bar{\xi}_e$ characterizes the material types with $\bar{\xi}_e = 1$ and $\bar{\xi}_e = 0$ indicating Material 1 and Material 2 for elements with $\bar{\rho}_e = 1$, respectively. A schematic illustration of such design parameterization is provided in Figure 2. The optimization design variables are $\boldsymbol{\rho}$ and $\boldsymbol{\xi}$, and the variables representing the physical structure are $\bar{\boldsymbol{\rho}}$ and $\bar{\boldsymbol{\xi}}$. The procedures of smoothing and projection, which map design variables to physical variables, are standard regularization techniques (i.e., three-field scheme) in topology optimization required to achieve a mesh-independent and near-discrete final designs. For more details about these techniques, see [31, 34]. We remark that, although we restrict our attention to composites with two material constituents in the above discussion, the concept is directly extendable to more than two material constituents.
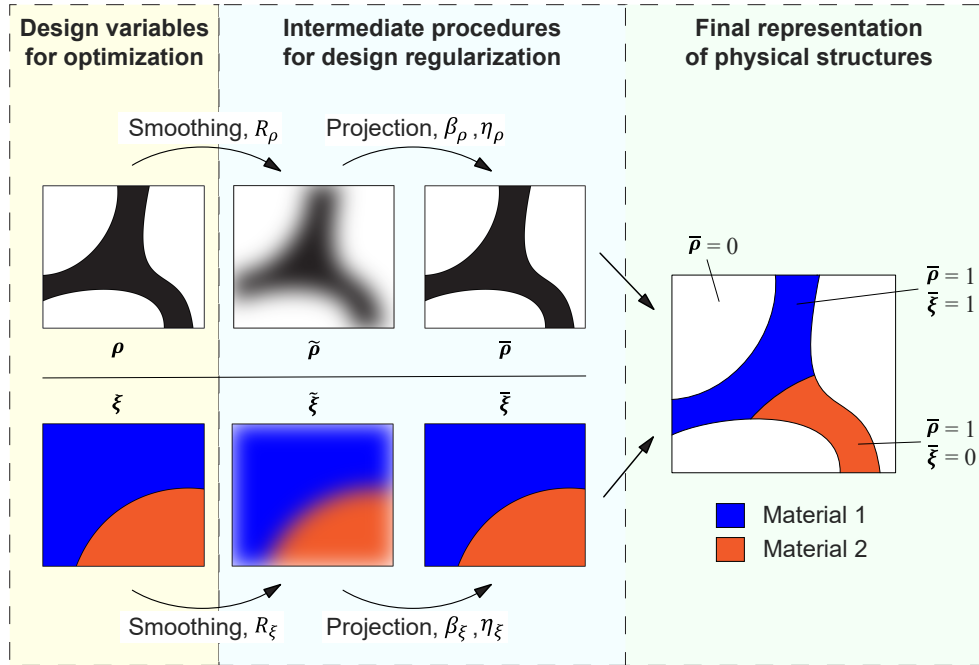

Figure 2: Design representation of a two-material structure using filtered and physical density and material variables.

We aim at obtaining near-discrete final designs with spatially exclusive solid materials with minimal mixing of phases and physically well-defined properties when $\bar{\rho}_e$ and $\bar{\xi}_e$ are close to 0 or 1. In Appendix D, we verify the discreteness of all the optimized designs in this study and show that both the grayness and the mixing of solid materials are below $< 1\%$.

3.1.2. Interpolations of the stored energy functions, stress tensors, and stress limits

The key to characterize the mechanical behavior of multi-material structures lies in the interpolation of the stored energy function through the two physical variables $\bar{\rho}_e$ and $\bar{\xi}_e$. The stored energy function of a two-material structure at a point in element e is interpolated as [33, 35]:

$$W_e\left(\bar{\rho}_e, \bar{\xi}_e, \gamma_e, \boldsymbol{u}_e\right) = \left[\epsilon_p + (1 - \epsilon_p)\,\bar{\rho}_e^{p_\rho}\right] \left[\bar{\xi}_e^{\,p_\xi} W_e^{(1)}\left(\gamma_e, \boldsymbol{u}_e\right) + \left(1 - \bar{\xi}_e\right)^{p_\xi} W_e^{(2)}\left(\gamma_e, \boldsymbol{u}_e\right)\right], \tag{8}$$

where p_ρ and p_ξ are the SIMP [31, 36] penalization parameters, $\epsilon_p = 10^{-6}$ is a small number to avoid singular state equation. To prevent severe element distortion and numerical instability in low-density regions, the interpolation approach proposed in [25] is employed to interpolate the stored energy function $W_e^{(j)}$ of material phase j as

$$W_e^{(j)}\left(\gamma_e, \boldsymbol{u}_e\right) = \hat{W}^{(j)}\left(\gamma_e \boldsymbol{u}_e\right) - W_L^{(j)}\left(\gamma_e \boldsymbol{u}_e\right) + W_L^{(j)}\left(\boldsymbol{u}_e\right), \tag{9}$$

where $\hat{W}^{(j)}\left(\cdot\right)$ is the hyperelastic stored energy function of Material j (introduced in Section 2), and $W_L^{(j)}$ is a linear elastic stored energy function of the form $W_L^{(j)}\left(\boldsymbol{u}_e\right) = \frac{1}{2}\boldsymbol{\epsilon}\left(\boldsymbol{u}_e\right) : \mathbb{C}^{(j)} : \boldsymbol{\epsilon}\left(\boldsymbol{u}_e\right)$ with $\mathbb{C}^{(j)}$ being the (plane stress) linear elasticity tensor of material j under small deformation theory, and $\boldsymbol{\epsilon}\left(\boldsymbol{u}_e\right)$ being the linear strain tensor. The interpolation factor γ_e is defined as

$$\gamma_e\left(\bar{\rho}_e\right) = \frac{\tanh(\beta_\gamma \rho_0) + \tanh\left(\beta_\gamma\left(\bar{\rho}_e^{p_\rho} - \rho_0\right)\right)}{\tanh(\beta_\gamma \rho_0) + \tanh(\beta_\gamma(1 - \rho_0))}, \tag{10}$$

where ρ_0 is the projection threshold and is set to 0.01, and β_γ is set to 500. According to the above expression, $\gamma_e \approx 1$ when $\bar{\rho}_e > \rho_0$ and the corresponding element is modeled as hyperelastic materials with stored energy function $\hat{W}^{(j)}$. On the other hand, $\gamma_e \approx 0$ when $\bar{\rho}_e < \rho_0$ and the corresponding element is modeled as linear elastic materials with stored energy function $W_L^{(j)}$. We emphasize that in the final near-discrete optimized designs, the parameter γ_e is 1 in solid regions and 0 in void regions as a result of the Heaviside projection (10) with $\beta_\gamma = 500$. Therefore, the behavior of the final design is governed by the objective and physically well-defined nonlinear stored-energy functions $\hat{W}^{(j)}$, and the linear stored-energy function $\hat{W}_L^{(j)}$ has a negligible impact on the final design as it is associated with void regions only. The energy interpolation scheme (9) that effectively alleviates numerical instabilities induced by low stiffness elements has been verified to have negligible influence on the performance of final optimized single-material designs in [25]. We further provide a numerical verification on a two-material design in Appendix B.

The interpolated stored energy function (8) (together with (9) and (10)) captures the mechanical behavior of the composite structure and is consistent with the schematic illustration in Figure 2. It can be seen that: 1) an element with $\bar{\rho}_e = 1$ and $\bar{\xi}_e = 1$ corresponds to Material 1, i.e. $W_e\left(1, 1, 1, \boldsymbol{u}_e\right) = \hat{W}^{(1)}\left(\boldsymbol{u}_e\right)$; 2) an element with $\bar{\rho}_e = 1$ and $\bar{\xi}_e = 0$ corresponds to Material 2, i.e. $W_e\left(1, 0, 1, \boldsymbol{u}_e\right) = \hat{W}^{(2)}\left(\boldsymbol{u}_e\right)$; and 3) an element with $\bar{\rho}_e = 0$ corresponds to void (with ersatz stiffness to avoid singular state equation), i.e., $W_e\left(0, \bar{\xi}_e, 0, \boldsymbol{u}_e\right) \approx \epsilon_\rho$.

To prevent the appearance of thin members and unrealistically large deformation concentration in the optimized designs, we propose a novel stress constraint for two-material structures that accounts for both distinct nonlinear behaviors and strength requirements of different materials through interpolation. The

6

interpolated Cauchy stress tensor of the multi-material structure for element e derived based on (8)–(9) is:

$$\boldsymbol{\sigma}\left(\bar{\rho}_e, \bar{\xi}_e, \gamma_e, \boldsymbol{u}_e\right) = \left[\epsilon_p + (1 - \epsilon_p)\,\bar{\rho}_e^{p_\rho}\right]\left[\bar{\xi}_e^{p_\xi}\boldsymbol{\sigma}^{(1)}\left(\gamma_e, \boldsymbol{u}_e\right) + \left(1 - \bar{\xi}_e\right)^{p_\xi}\boldsymbol{\sigma}^{(2)}\left(\gamma_e, \boldsymbol{u}_e\right)\right], \qquad (11)$$

where $\boldsymbol{\sigma}^{(j)}\left(\gamma_e, \boldsymbol{u}_e\right)$ is the Cauchy stress tensor associated with Material j given by:

$$\boldsymbol{\sigma}^{(j)}\left(\gamma_e, \boldsymbol{u}_e\right) = \boldsymbol{\sigma}_{NL}^{(j)}\left(\gamma_e\boldsymbol{u}_e\right) + (1 - \gamma_e)\,\boldsymbol{\sigma}_L^{(j)}\left(\boldsymbol{u}_e\right), \qquad (12)$$

with $\boldsymbol{\sigma}_{NL}^{(j)}$ and $\boldsymbol{\sigma}_L^{(j)}$ being the nonlinear and linear parts of the Cauchy stress based on the interpolation scheme (9) given by:

$$\boldsymbol{\sigma}_{NL}^{(j)}\left(\gamma_e\boldsymbol{u}_e\right) = \frac{1}{J\left(\gamma_e\boldsymbol{u}_e\right)}\boldsymbol{F}\left(\gamma_e\boldsymbol{u}_e\right)\boldsymbol{S}^{(j)}\left(\gamma_e\boldsymbol{u}_e\right)\boldsymbol{F}^T\left(\gamma_e\boldsymbol{u}_e\right) \ \text{and}\ \boldsymbol{\sigma}_L^{(j)}\left(\boldsymbol{u}_e\right) = \mathbb{C}^{(j)} : \boldsymbol{\epsilon}\left(\boldsymbol{u}_e\right). \qquad (13)$$

In the above expressions, $\boldsymbol{S}^{(j)}$ is the 2nd PK stress associated with Material j, which is calculated from $\hat{W}^{(j)}$. We note that the interpolated Cauchy stress tensor in Eq. (11) recovers the Cauchy stress of Material 1 when $\bar{\rho}_e = 1$ and $\bar{\xi}_e = 1$, i.e. $\boldsymbol{\sigma}\left(1, 1, 1, \boldsymbol{u}_e\right) = \boldsymbol{\sigma}_{NL}^{(1)}\left(\boldsymbol{u}_e\right)$; and reduces to the Cauchy stress of Material 2 when $\bar{\rho}_e = 1$ and $\bar{\xi}_e = 0$, i.e. $\boldsymbol{\sigma}\left(1, 0, 1, \boldsymbol{u}_e\right) = \boldsymbol{\sigma}_{NL}^{(2)}\left(\boldsymbol{u}_e\right)$. In addition, the interpolated Cauchy stress tensor in Eq. (11) gives $\boldsymbol{\sigma}\left(0, \bar{\xi}_e, 0, \boldsymbol{u}_e\right) = \boldsymbol{0}$ (neglecting ϵ_ρ) in the void region with $\bar{\rho}_e = 0$.

In the proposed stress constraint, we adopt the von Mises stress as the measure to control the level of deformation as it is closely related to distortional deformation. In Appendix C, we demonstrate the proposed stress constraint with von Mises stress to be effective in eliminating excessive deformations and thin members. We note that the von Mises stress is used as an effective design tool to control the deformation level rather than the indicator of materials' physical failure, and other stress-based failure criteria for soft materials can also be employed in the proposed stress constraint. The interpolated von Mises stress limit for the two materials is defined as:

$$\bar{\sigma}\left(\bar{\rho}_e, \bar{\xi}_e\right) = \left[\epsilon_q + (1 - \epsilon_q)\,\bar{\rho}_e^{q_\rho}\right]\left[\bar{\xi}_e^{q_\xi}\bar{\sigma}^{(1)} + \left(1 - \bar{\xi}_e\right)^{q_\xi}\bar{\sigma}^{(2)}\right], \qquad (14)$$

where $\bar{\sigma}^{(j)}$ is the assigned von Mises stress limit for Material j, and $\epsilon_q = 10^{-6}$. To prevent singularity issues in stress constrained topology optimization, relaxation approach is generally needed [37, 38]. The relaxation can be achieved by letting $q_\rho < p_\rho$ and $q_\xi < p_\xi$ [39]. This work uses $q_\rho = p_\rho - 0.5$ and $q_\xi = p_\xi - 0.5$. Similar to the stress interpolation, when $\bar{\rho}_e = 1$ and $\bar{\xi}_e = 1$, (14) recovers $\bar{\sigma}\left(1, 1\right) = \bar{\sigma}^{(1)}$; when $\bar{\rho}_e = 1$ and $\bar{\xi}_e = 0$, $\bar{\sigma}\left(1, 0\right) = \bar{\sigma}^{(2)}$; and when $\bar{\rho}_e = 0$, $\bar{\sigma}\left(0, \bar{\xi}_e\right) = 0$ neglecting the ϵ_q.

3.2. Multi-material design optimization formulation

We formulate the design of a multi-material structure with a prescribed force-displacement curve as minimizing the maximum errors between the actual and the prescribed curve for a given range of loaded

7

displacement:

$$\min_{\boldsymbol{\rho},\boldsymbol{\xi}} \left\{ \max_{d_i} \left(\frac{f(d_i) - f^*(d_i)}{\bar{f}} \right)^2 + \theta \frac{\boldsymbol{v}^T \bar{\boldsymbol{\rho}}}{\bar{v}} \right\}, \quad i = 1, ..., n$$

$$\text{s.t.} \quad \boldsymbol{r}\left(\bar{\boldsymbol{\rho}}, \bar{\boldsymbol{\xi}}, \boldsymbol{u}^i\right) = \boldsymbol{0}, \quad i = 1, ..., n$$

$$\boldsymbol{v}^T \bar{\boldsymbol{\rho}} \leq \bar{v}$$

$$\left\{ \sum_{e=1}^{N} \left[\frac{\frac{1}{v_e} \int_{\Omega_e} \sigma^{VM}\left(\boldsymbol{\sigma}\left(\bar{\rho}_e, \bar{\xi}_e, \gamma_e, \boldsymbol{u}_e^n\right)\right) \, \mathrm{d}\boldsymbol{x}}{\bar{\sigma}\left(\bar{\rho}_e, \bar{\xi}_e\right)} \right]^p \right\}^{\frac{1}{p}} \leq 1 \tag{15}$$

$$\boldsymbol{0} \leq \boldsymbol{\rho} \leq \boldsymbol{1}$$

$$\boldsymbol{0} \leq \boldsymbol{\xi} \leq \boldsymbol{1}$$

where N is the total number of elements in the finite element mesh, d_i is the ith displacement control point in the assigned displacement range $[d^0, d^1]$, $f(d_i)$ and $f^*(d_i)$ are the actual and prescribed forces at control point d_i, $\bar{f}$ is the averaged prescribed force $\bar{f} = 1/n \sum_{j=1}^{n} f^*(d_j)$, n is the total number of control points, $\boldsymbol{v}$ is the element volume vector, $\bar{v}$ is the assigned maximum volume for materials, $\boldsymbol{u}^i$ is the displacement vector at the ith control point, and θ is a volume penalization factor taken to be 0.01. The volume penalization term $\theta \boldsymbol{v}^T \bar{\boldsymbol{\rho}}/\bar{v}$ eliminates potential superfluous materials when the volume constraint is inactive. The stress constraint in the optimization formulation is expressed in quotient form, where the numerator is the averaged von Mises stress of element e, with $\sigma^{VM}(\cdot)$ denoting the von Mises stress function, $\boldsymbol{\sigma}$ defined in (11), and $\bar{\sigma}$ being the interpolated stress limit in (14). The stress constraint is handled by the p-norm approach [40] with $p = 16$.

Using the adjoint method, the sensitivity of a generic function ϕ with respect to the physical variable $\bar{\rho}_e$ and $\bar{\xi}_e$ can be computed as:

$$\frac{\partial \phi}{\partial \bar{\rho}_e} = \frac{\partial \phi\left(\bar{\boldsymbol{\rho}}, \bar{\boldsymbol{\xi}}, \boldsymbol{u}^i\right)}{\partial \bar{\rho}_e} + \boldsymbol{\lambda}^T \frac{\partial \boldsymbol{r}\left(\bar{\boldsymbol{\rho}}, \bar{\boldsymbol{\xi}}, \boldsymbol{u}^i\right)}{\partial \bar{\rho}_e} \quad \text{and} \quad \frac{\partial \phi}{\partial \bar{\xi}_e} = \frac{\partial \phi\left(\bar{\boldsymbol{\rho}}, \bar{\boldsymbol{\xi}}, \boldsymbol{u}^i\right)}{\partial \bar{\xi}_e} + \boldsymbol{\lambda}^T \frac{\partial \boldsymbol{r}\left(\bar{\boldsymbol{\rho}}, \bar{\boldsymbol{\xi}}, \boldsymbol{u}^i\right)}{\partial \bar{\xi}_e}, \tag{16}$$

respectively, and $\boldsymbol{\lambda}$ is the adjoint vector obtained through solving the adjoint system:

$$\boldsymbol{K}^T\left(\bar{\boldsymbol{\rho}}, \bar{\boldsymbol{\xi}}, \boldsymbol{u}^i\right) \boldsymbol{\lambda} = -\frac{\partial \phi\left(\bar{\boldsymbol{\rho}}, \bar{\boldsymbol{\xi}}, \boldsymbol{u}^i\right)}{\partial \boldsymbol{u}^i}, \tag{17}$$

with $\boldsymbol{K}^T\left(\bar{\boldsymbol{\rho}}, \bar{\boldsymbol{\xi}}, \boldsymbol{u}^i\right) \doteq \partial^2 \Pi(\bar{\boldsymbol{\rho}}, \bar{\boldsymbol{\xi}}, \boldsymbol{u}^i)/\partial \boldsymbol{u}^2$ being the tangent stiffness matrix evaluated at $\boldsymbol{u}^i$. The above procedure ((16) and (17)) applies to both the objective and stress constraint functions. The sensitivity with respect to the design variable ρ_e and ξ_e can be obtained through (16)-(17) and chain rule [41, 34].

The parameter p_ρ is set as 3, and we use continuation strategies for parameters p_ξ (and therefore q_ξ), β_ρ, and β_ξ. Based on numerical experience, all the three parameters are initially set to 1, and the sequence of continuation is: 1) p_ξ is increased to 3 with a 0.5 increment every 40 steps starting at step 300 and ending at step 460; 2) β_ρ is doubled every 30 steps starting from step 460 until finishing as 64 at step 640; 3) β_ξ is doubled every 30 steps starting at step 640 until finishing as 64 at step 820. The continuations of β_ρ and β_ξ are not activated simultaneously to alleviate the perturbations of the optimization problem. We apply continuation of β_ρ before β_ξ in order to first achieve the near-discrete structural boundaries before realizing the near-discrete material interfaces. The min-max problem (15) is solved using the bound formulation [42] to circumvent the non-differentiability, and the Method of Moving Asymptotes (MMA) [43] is adopted to perform the iterative design variable update. The optimization is terminated when the change of the design

variables is smaller than the tolerance value 0.01 with the maximum step of 870 (which provides 50 additional steps after the parameter continuation finishes at step 820).

4. Numerical results

In this section, we use the proposed framework to design structures that achieve various prescribed nonlinear elastic responses. We consider a design domain with load and boundary conditions shown in Figure 3 **a**. The out-of-plane domain thickness is 2mm. We investigate three design scenarios under large deformations. Scenario 1 aims to achieve a linear force-displacement response with nonlinear materials; Scenario 2 aims to achieve a bi-linear one with hardening behavior; Scenario 3 aims to achieve a bi-linear force-displacement response that cannot be attained with either Material 1 or Material 2 alone. In each scenario, we consider two candidate materials of distinct nonlinear behaviors: Material 1 has a hardening behavior with a positive curvature in the stress-stretch curve, and Material 2 has a softening behavior with a negative curvature. The materials considered in this paper can be realized by silicon-based elastomers, e.g., polydimethylsiloxane (PDMS) [44]. The uniaxial stress-stretch curves and parameters of Material 1 and Material 2 for Scenarios 1 to 3 (in Figure 3 **b**–**d**) are chosen based on the uniaxial test results of PDMS with various base-agent compositions [44]. The ratio of the bulk modulus κ and shear modulus G is set to 500 to mimic the near-incompressible behavior of elastomers. The Material 1 used in Scenario 2 is chosen to be slightly stiffer than that used in Scenario 1 to accommodate the steeper slope in Curve C (Figure 3 **f**). In Scenario 3, we choose two materials with stress-stretch curves forming a cross to study the situation where using either material alone cannot achieve a target curve (see later elaboration). These material models are rank one convex within the range of stretch values in the two-material designs of this study. The corresponding target force-displacement curves are shown in Figure 3 **e**–**g**, respectively. For all scenarios, we use 10 control points (i.e., $n = 10$) and the maximum prescribed displacement is set as 40mm, which is 40% of the domain height H. The optimized designs are dependent on initial guesses because of the non-convex nature of the optimization problem (15). Thus, for each scenario, we investigate four initial guesses of $\boldsymbol{\rho}$ shown in Figure 3 **h**-**k** (same setup for both 1:1 and 1.5:1 domains) and present the design with the smallest fitting error. The initial guesses of $\boldsymbol{\xi}$ are uniformly equal to 0.5 in all cases. To compare fitting errors of different optimized designs, we use the normalized maximum absolute error defined as $\max_{d_i} \left[f(d_i) - f^*(d_i) \right] / \bar{f}$ as the error measurement, which is the same quantity used in the objective function of (15). The discreteness of all optimized designs are examined by quantitative measures and is summarized in D.2.

To gain better insights on whether the force-displacement curve is attainable through optimization formulation (15), we plot in Figure 3 **e**-**g** the bounding curves of the force-displacement relations for Scenarios 1–3, respectively. Those curves serve as the estimated bounds of the maximum force-displacement curves achievable given the design parameters and material properties in each scenario. Each point on the bounding curve is obtained by solving a topology optimization problem to maximize the applied external force under a prescribed displacement value on the x-axis. Once the bounding curve is obtained, any force-displacement relation that goes above it is considered unachievable. This provides an indicator to rule out those unattainable force-displacement curves before the optimization 15 is performed. We note that the two bounding curves in each scenario have similar shapes with the material stress-stretch curves under uniaxial tension because of the tension-dominated structural behavior in the example setup (Figure 3 **a**). Because the two material behaviors in Scenario 3 form a cross, we further plot the two-material bounding curve, which indicates a higher achievable maximum force-displacement response when using two materials.
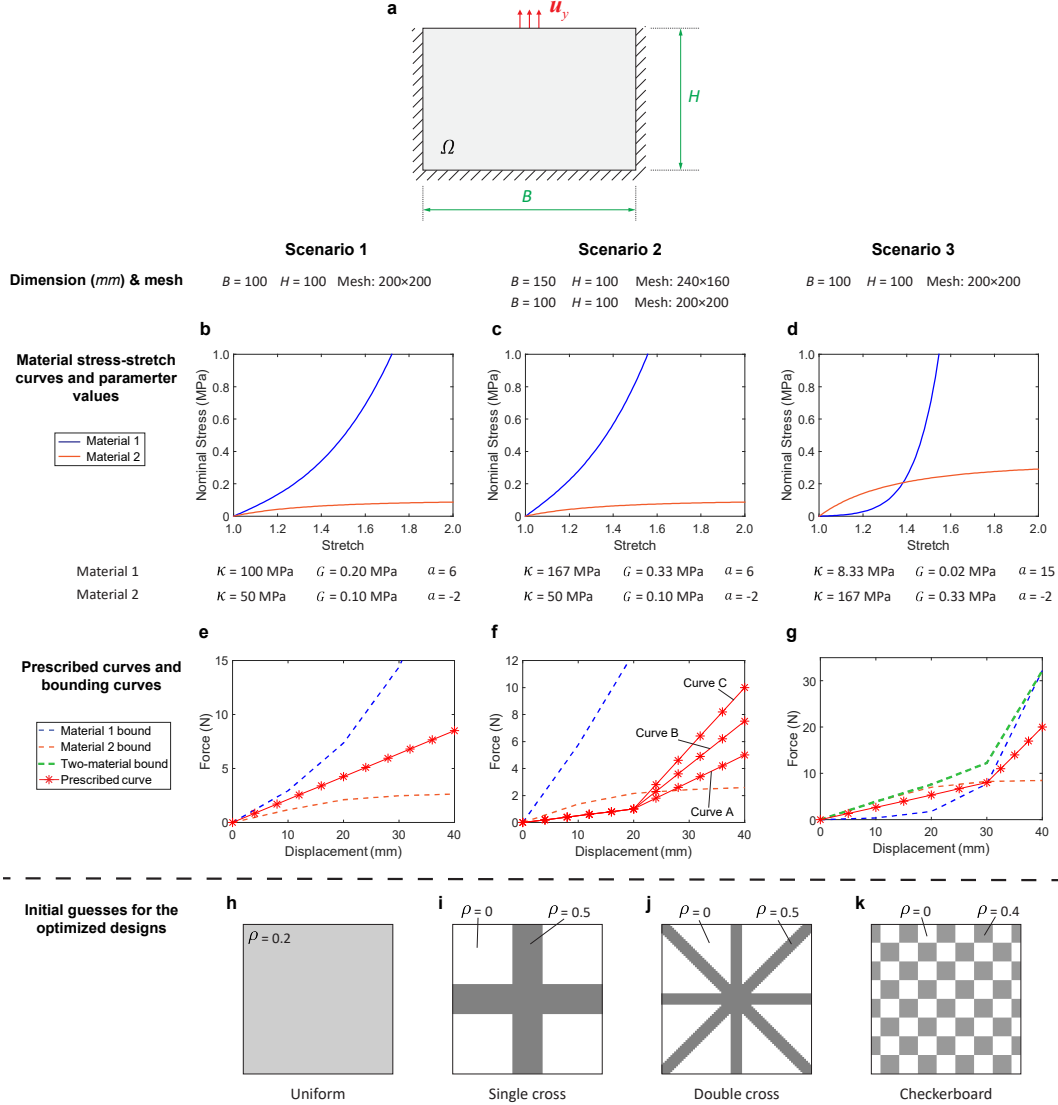
9

Figure 3: (a) Design domains, boundary conditions, dimensions, and FE mesh sizes; (b)–(d) uniaxial stress-stretch curves of the three sets of materials and associated material parameters corresponding to the three scenarios (shapes and magnitudes are chosen based on test results of silicon-based elastomer PDMS); (e)–(g) bounding curves and prescribed force-displacement curves for the three scenarios; (h)–(k) initial guesses of $\boldsymbol{\rho}$.

4.1. Scenario 1: linear force-displacement response with nonlinear materials under finite deformations

This scenario aims to design structures that harness highly nonlinear materials to achieve a linear force-displacement curve under large deformations. The target linear force-displacement curve is shown in Figure 3 **e**, which lies between the bounding curves of the two candidate materials. For this target force-displacement curve, considering only single material (i.e., either Material 1 or Material 2) in the optimization leads to optimized designs with poor fitting quality. Figure 4 shows the single-material optimized structures (with uniform initial guess, Figure 3 **h**) and the comparisons of their actual force-displacement curves versus the target one. The optimized structure obtained by considering Material 1 alone achieves a force-displacement curve having similar magnitude to the target one with a normalized maximum error of 0.185. However, an apparent positive curvature appears in the actual force-displacement curve, which is inherited from the stress-stretch curve of Material 1. On the other hand, the optimized design obtained by considering Material

10

2 alone achieves a force-displacement curve that is far below the target one with the normalized maximum error being 1.260. This is expected because, unlike Material 1, the bounding curve of Material 2 suggests that the target force-displacement curve is unattainable by only considering Material 2.
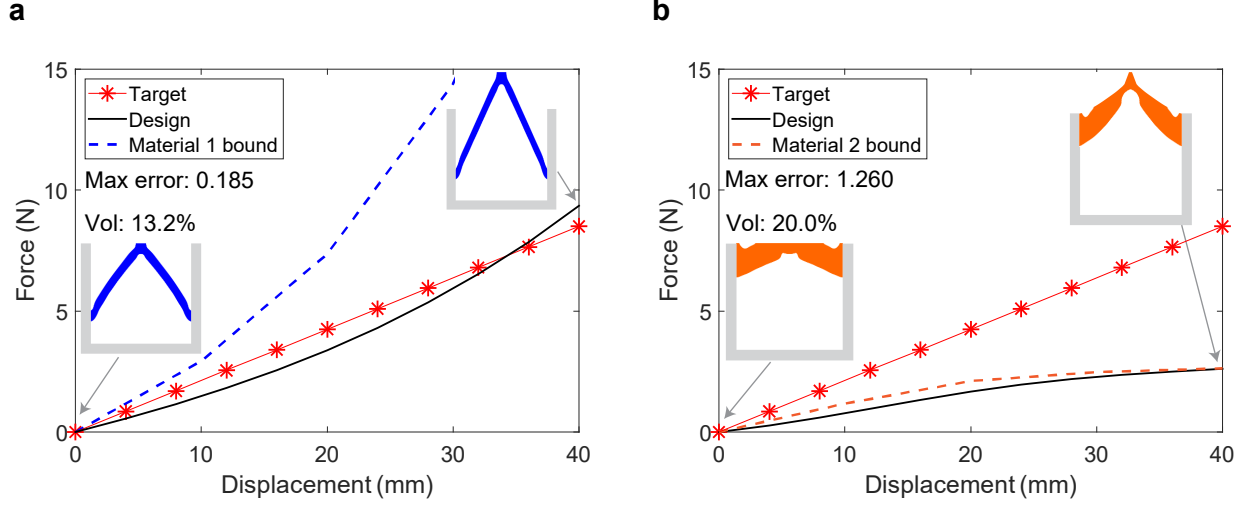

Figure 4: Scenario 1 using single material: (a) Optimized design and fitting of force-displacement curve for case using only Material 1; (b) optimized design and fitting of force-displacement curve for case using only Material 2.
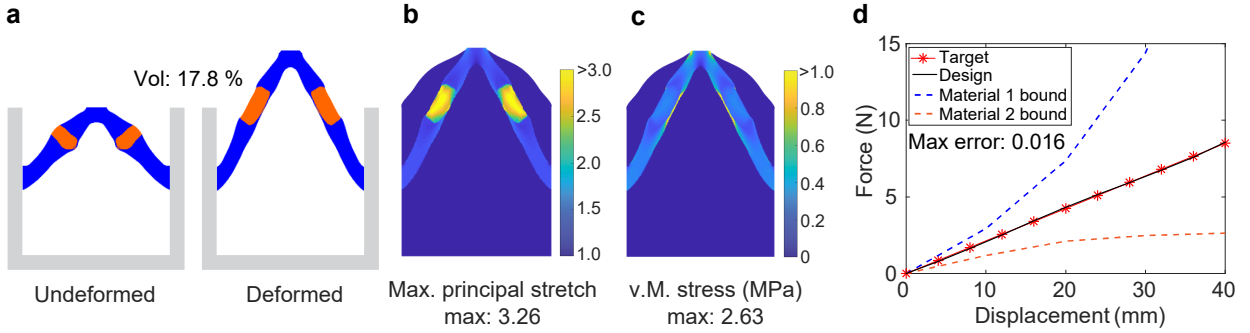
Figure 5: Scenario 1 using both Material 1 and Material 2: (a) Optimized design; (b) maximum principal stretch; (c) von Mises stress; (d) fitting of force-displacement curve.

To enlarge the design space and achieve the prescribed curve, the use of both materials is necessary. We demonstrate that, by harnessing two highly nonlinear materials, i.e., using both Material 1 and Material 2 in the optimization, a linear force-displacement structural response under large deformation is attainable. The stress limits for both Material 1 and Material 2 are chosen as 6MPa. Figures 5 **a** and **d** show the optimized design (with the uniform initial guess, Figure 3 **h**) and the comparison between the actual and target force-displacement curves, respectively. Both candidate materials appear in the optimized design, leading to a composite structure composed of two straight members that deform in a stretch-dominated pattern. In each member, Material 2 appears in the middle, and Material 1 shows up at the top and bottom, forming a system similar to the "springs in series". In addition, the final volume fraction of the optimized composite structure is 17.8% (lower than 20% prescribed upper bound), showing that the material usage is also optimized to achieve the prescribed force-displacement curve.

The fringe plots of principal stretch and von Mises stress distributions in the optimized composite design

11

are provided in Figures 5 **b** and **c**, respectively. From both fringe plots, we observe that the stress constraint is effective in limiting the deformation and stress levels in the optimized design to prevent local material failure, which we found could otherwise happen without the stress constraint. According to the stretch fringe plot, deformation localizes in the Material 2 regions with a maximum stretch of 3.26. For Material 1, the stretch is lower than 1.7 in most regions. These levels of stretch can be achieved by typical elastomers without failure (see [45]). From the von Mises stress fringe plot, the distribution of von Mises stress is relatively uniform along most areas of two branches, and the highest von Mises stress appears in the thin strip made of Material 1 with a value of 2.63MPa. The localization of deformation and the relative uniformity of stress are typical behaviors of the "springs in series" system composed of springs with distinct stiffness.

The fitting quality of the composite structure is considerably better than the ones obtained using only single materials. As shown in Figure 5 **d**, the actual force-displacement curve of the optimized composite structure is almost perfectly linear and has a normalized maximum error of 0.016. The linearity comes from the optimized material composition and the serial layout of the two materials with hardening (Material 1) and softening (Material 2) behaviors, resulting in a collectively linear behavior. Both the material and geometric nonlinearities have contributed to forming the linear force-displacement response. Comparing with the optimized designs obtained by single materials, the significantly reduced fitting error achieved by the optimized composite structure (0.016 versus 0.185 and 1.260 in the single-material cases) showcases the enhanced capability of the multi-material topology optimization in programming a wider spectrum of force-displacement responses than the single-material one.

4.2. Scenario 2: bi-linear force-displacement responses with hardening behavior

The second scenario aims to design structures by exploiting the geometric variations to achieve three bi-linear force-displacement curves with hardening behaviors. We also investigate the influences of domain aspect ratios and initial guesses on the designs. The three bi-linear curves, as shown in Figure 3 **f**, have the same initial low-stiffness region (for displacement < 20 mm) followed by hardening regions with increasing slopes. We first use a 1.5 : 1 design domain to investigate these three target bi-linear curves. We then restrict our attention to the curve with the most hardening response (i.e., Curve C) and use a 1:1 design domain to explore different initial guesses. We show that the optimization leads to mechanism-like structures that change their deformation modes from flexure-dominated to stretch-dominated to realize the hardening. We also show that there exist multiple structures with distinct geometries that achieve fairly accurate fits to the same prescribed curve. For this design scenario, we set the respective stress limit for Material 1 and Material 2 to be 5MPa and 0.5MPa for Curves A, B, and C.

Figure 6 shows optimized designs (both undeformed and deformed configurations) that achieve three target bi-linear curves, their stretch fringe plots, and corresponding fitting of the force-displacement responses. For each curve, we test the four initial guesses (Figure 3 **h** – **k**) and present the design with lower fitting errors in Figure 6 (**a** and **b** are obtained with the checkerboard and **c** are from the uniform initial guess).

All three optimized designs exhibit a similar mechanism, which transits from a flexure-dominated deformation to a stretch-dominated one, to achieve the bi-linear hardening force-displacement curves. Comparing the overall shapes of three optimized designs, they have similar topology that resemble a frog, and the deformed configurations resemble a "jumping frog". The "legs" first undergo flexure-dominated deformations to unfold themselves, producing the initial region of the force-displacement with the small slope. As the "legs" gradually become straight, they start to undergo stretch-dominated deformations to achieve the hardening responses in the second part of three curves. The "legs" have hinge-like joints with high deformation concentration (as shown in all three maximum stretch plots in Figure 6) to form the mechanism-like behavior.

12

In terms of the differences in the topology and consumed volume, as the second part of the target curve becomes stiffer from Curve A to Curves B and C, the "legs" in the three optimized designs become thicker so as to achieve a stronger hardening response, and the final volume fraction of the designs increases from 10.9% to 16.6% and 20%, respectively. This suggests that more intensive hardening curve may require a higher amount of material to form the thicker bottom members.
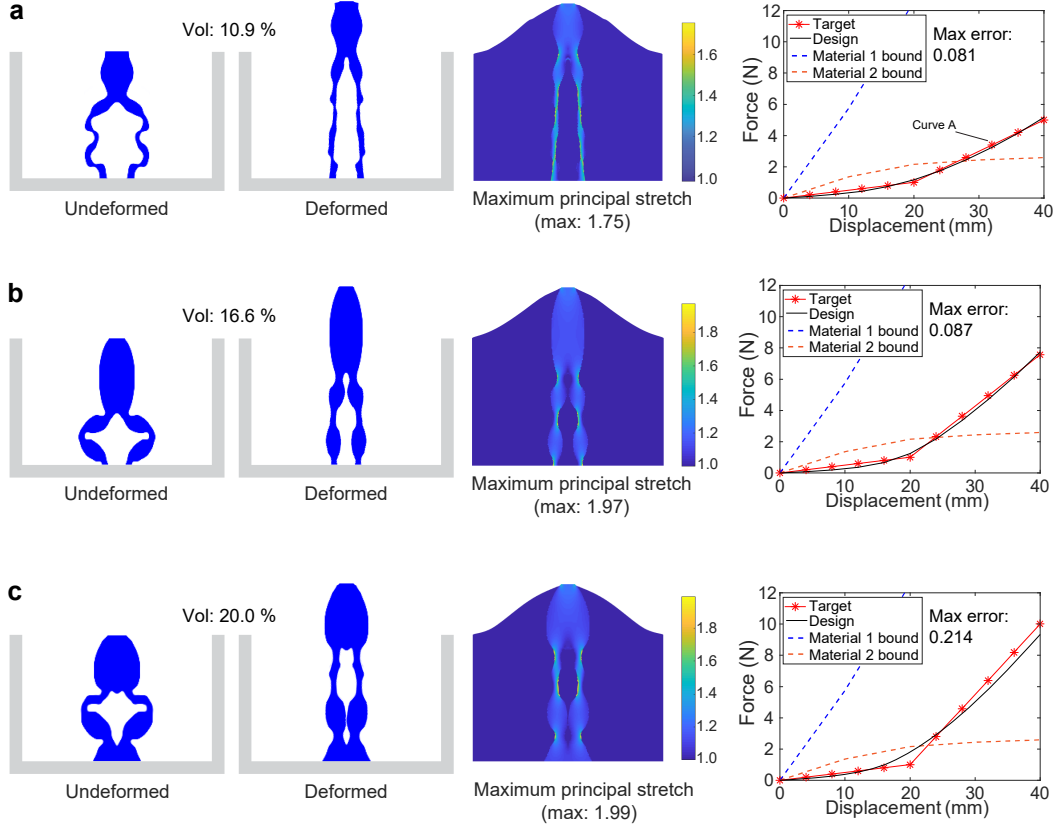

Figure 6: Scenario 2 (1.5:1 design domain) with three target curves. Optimized designs, maximum principal stretches, and fittings of force-displacement curves for (a) target Curve A; (b) target Curve B; (c) target Curve C; respectively.

Notably, the optimization leads to three designs using mostly Material 1, indicating geometric variations (rather than mixing multiple given materials) are exploited in this scenario to achieve the bi-linear target curves with hardening responses, which is in agreement with the hardening behavior of Material 1. In terms of fitting quality, the normalized absolute errors of the three optimized designs are 0.081, 0.087, and 0.214, respectively. The normalized maximum error of the optimized design for Curve C occurs at the control point at the kink (the transition point between two slopes). Because the actual force-displacement curves are usually smooth, the poor fit at the kink is expected. Moreover, curves with more hardening have a more drastic change of the discontinuous slopes, and thus, are more difficult to fit. Finally, the optimized design in Curve C reaches the 20% prescribed maximum volume limit and has a larger fitting error than the other two designs with less hardening, this may indicate that a larger material usage in the design could potentially enhance the hardening behavior and hence improve the fitting.
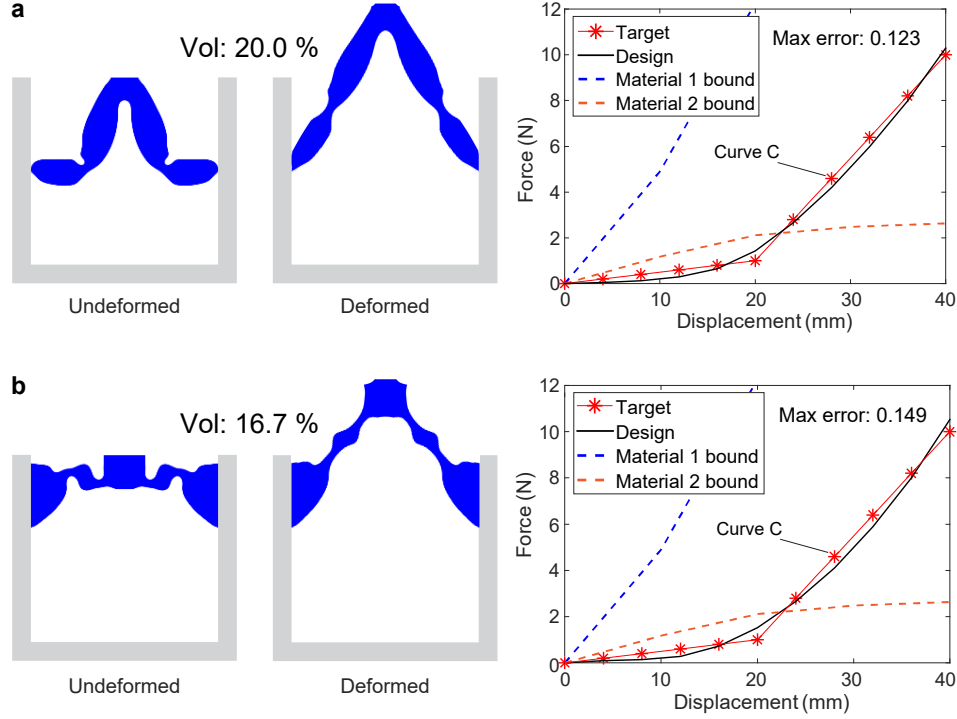
Figure 7: Scenario 2 with Curve C (1:1 design domain) using two initial guess cases. (a) Optimized design and fitting of force-displacement curve using "double cross" initial guess (Figure 3 **j**); (b) optimized design and fitting of force-displacement curve using "checkerboard" initial guess (Figure 3 **k**).

Next, we use target Curve C to study a different domain size (with a smaller width-to-height ratio) and various initial design configurations (initial guesses). We consider a 1:1 design domain using the same materials with four initial guesses (in Figure 3) and present results from the "double cross" and "checkerboard" as these two initial guesses result in the lowest fitting errors, as shown in Figure 7. For both designs, the stress constraints are inactive and the maximum stretch values are below 3.1. Different from the topology obtained using the wider 1.5:1 domain (Figure 6 **c**), both designs from the narrower 1:1 domain are attached to the side supports instead of the bottom, which is a result of the shorter distance between the loading area and side supports, allowing for a more efficient use of materials toward the side. Although having different topology from the one in the 1.5:1 domain, the optimized designs in the 1:1 domain exhibit similar mechanisms, i.e., the flexure-to-stretch deformation mode, to achieve the target bi-linear force-displacement curve. In addition, better fitting quality is obtained with the 1:1 ratio design domain, with the normalized maximum error in force being 0.123 and 0.149. Finally, the distinct optimized designs from different initial guesses are manifestation of the non-convexity of the optimization problem, where multiple local optima exist. The proposed formulation with non-convexity enables the exploration of a variety of distinct designs that achieve the same programmed nonlinear elastic behaviors by employing different initial guesses and domain sizes, which has merit from a design perspective.

4.3. Scenario 3: bi-linear force-displacement response unachievable by a single material

The third scenario aims to demonstrate that harnessing multiple materials can enlarge the programmable force-displacement space and lead to structures with force-displacement curves that are physically unachievable using either of the candidate material alone. The target force-displacement curve is a bi-linear one shown

14

in Figure 3 **g**. Materials 1 and 2 considered in this example form an intersection in the corresponding bounding curves. Different from the ones in Scenario 2, the target curve considered here is physically unattainable by neither Material 1 nor Material 2, as it contains regions above the bounding curves of both Material 1 and Material 2. The target curve before the intersection of two bounding curves is above the Material 1 bound and hence unachievable for structures with only Material 1. The target curve after the intersection is above the Material 2 bound and hence unreachable for structures made of only Material 2. This is further verified by numerical results presented in Figure 8 (designs are obtained with the uniform initial guess, Figure 3 **h**), which show poor fittings of the single-material designs. As shown in Figure 8, because the bounding curves of both Material 1 and Material 2 are partially below the target curve, the actual curves of the single material designs have poor fittings to the targets (since the actual force-displacement curves cannot exceed the bounding curves). For the design with Material 1 alone (Figure 8 **a**), the actual curve has a large discrepancy with the target curve when displacement < 30mm. The optimized design considering Material 1 alone has a normalized maximum error of 0.413. For the design with Material 2 alone (Figure 8 **b**), the actual curve matches well with the target before displacement reaches 30mm, but a large discrepancy appears after 30mm because the bounding curve of Material 2 is far below the target curve. The optimized design considering Material 2 alone has a normalized maximum error of 1.272.
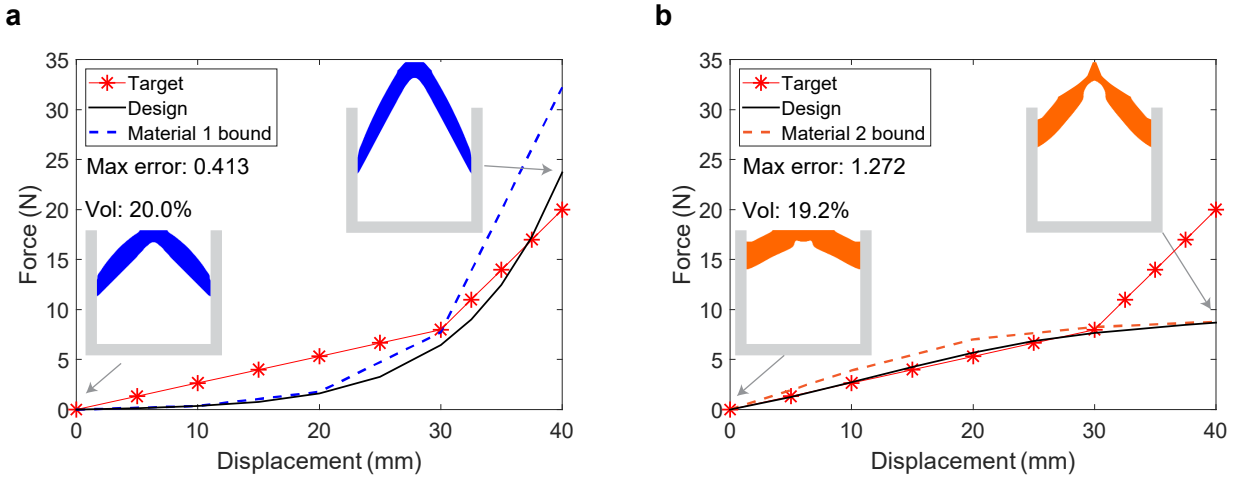

Figure 8: Scenario 3 using single materials: (a) Optimized design and fitting of force-displacement curve for case using only Material 1; (b) optimized design and fitting of force-displacement curve for case using only Material 2.
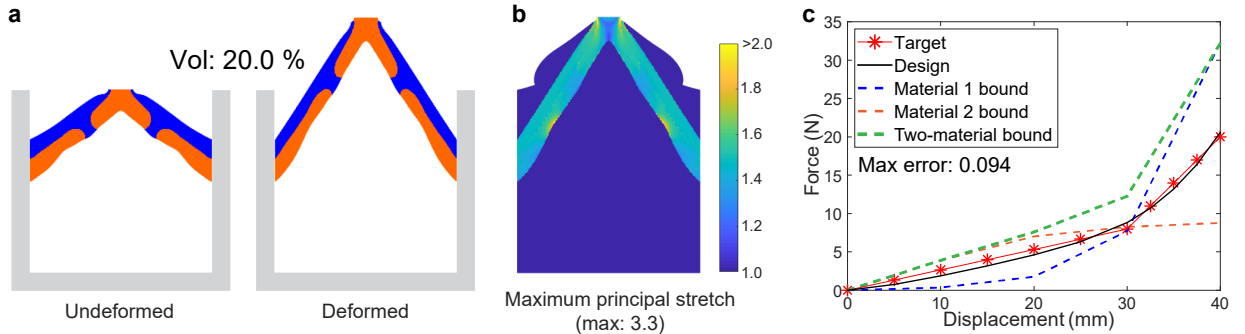

Figure 9: Scenario 3 using multi-material: (a) Optimized design obtained by using Material 1 and Material 2; (b) maximum principal stretch; (c) fitting of force-displacement curve.

By incorporating both Material 1 and Material 2 in the optimization, the target force-displacement curve is achievable as it is within the two-material bounding curve (Figure 9 **c**). Figure 9 shows the optimized composite design (in both undeformed and deformed configurations), maximum stretch plots, and fitting curve obtained with the uniform initial guess (Figure 3 **h**). The final volume fraction of the optimized composite structure is 20%, which uses all available materials. As expected, both Material 1 and Material 2 are present in the optimized design, which is composed of two straight members deforming in a stretch-dominated pattern. The material distribution in each member resembles a system that combines a dominant portion of "springs in parallel" and a small portion of "springs in series". As shown in Figure 9 **b**, the distribution of principal stretch in the optimized design is mostly uniform (although some deformation concentrates around the location where the displacement loading is prescribed due to the boundary effect), which agrees with the major feature of the dominated "springs in parallel" arrangement. Above-mentioned observations are different from the ones made for the optimized design in Scenario 1, where a "springs in series" system is formed with apparent deformation localization in the weak material (i.e., Material 2) regions.

The fitting quality of the force-displacement curve is greatly improved, with a normalized maximum error of 0.094 as shown in Figure 9 **c**. In addition, the two-material bounding curve (green dashed curve) is above the envelope of the bounds of Material 1 and Material 2, which indicates a higher achievable maximum force-displacement response and a larger design space when using two materials compared to a single material. The observation explains the fact that the actual force-displacement curve is slightly above the single material bounds at 30 mm displacement. The lower fitting error and higher achievable maximum response demonstrate that harnessing multiple candidate materials enlarges the design space and thus provides the capability of programming a wider spectrum of responses than considering one material.

5. Concluding remarks

In this work, we systematically design composite structures with programmable elastic responses under large deformations through an effective multi-material topology optimization framework. The framework exploits multiple hyperelastic materials with distinct nonlinear elastic behaviors and formulates an inverse design problem to optimize both the topology and material distribution of a composite structure to achieve target force-displacement curves. A novel stress constraint function that accounts for two materials with distinct nonlinear elastic constitutive relations and different stress limits is proposed and shown to be effective in controlling the deformation levels and eliminating potential thin members in the optimized designs. Three design scenarios are presented which use the proposed multi-material framework to reveal unique structures with various programmable force-displacement curves under large deformation, including a linear curve, several bi-linear curves with hardening response, and a bi-linear curve that is unachievable by single-material designs. By comparing the designs obtained between single- and multi-material topology optimization, we demonstrate that harnessing multiple materials can lead to designs with better fitting and achieving a wider range of target responses.

The optimized designs reveal distinct mechanisms, unconventional geometric variations, and proper material distributions to achieve programmed force-displacement target curves. For the linear target curve, the design that harnesses two nonlinear candidate materials, forms a "springs in series" system with localized deformation in weak material and experiences a stretch-dominated deformation mode to achieve the linear structural response. For three bi-linear curves with small initial stiffness and increasing hardening behaviors, the single-material designs consisting of mostly the hardening material (Material 1) with distinct geometries

16

are obtained, suggesting geometrical variations are exploited to realize such type of target curves. The optimized designs exhibit mechanism-like behaviors, which experience transitions from flexure-dominated to stretch-dominated deformation modes, to achieve the sudden hardening behavior. Furthermore, increasing the hardening slopes of the prescribed curves result in an increase use of materials to form thicker bottom members exploiting similar mechanisms. By employing different initial design configurations, we obtain multiple designs achieving the same programmed nonlinear elastic behaviors. For the bi-linear curve that is unachievable by single-material (Scenario 3), the optimized design makes use of both candidate materials, forming a system that combines a dominant portion of "springs in parallel" and a small portion of "springs in series", leading to a uniform distribution of deformation with a stretch-dominated mode, which results in an accurate fitting of the target curve.

We remark that the manufacturing of the optimized designs and experimental validations of the programmed structures are crucial and part of our on-going research. Manufacturing of composite structures is in general challenging from two main aspects: 1) how to accurately manufacture different parts of structures occupied by different materials with irregular geometries and, 2) how to ensure the strength of interfacial bonding between the two materials to prevent premature interfacial failure when loaded. These two challenges shall be addressed through innovative manufacturing procedures.

Finally, we remark that, while this study focuses on hyperelastic materials with loading conditions being mostly tension-dominated, extensions to more complex loading scenarios and other types of target curves as well as incorporation of other material behaviors are promising areas for future studies. Additionally, we note that while this work focuses on two-dimensional structures, the framework can be extended to three-dimensional designs, which is planned for future research. The computational cost as well as the difficulty of manufacturing three-dimensional optimized structures could increase drastically.

Appendix A. Alternative formulation and results

The optimization formulation (15) proposed in the paper aims to minimize the normalized maximum absolute errors between the actual and prescribed force-displacement curves, as the normalization factor $\bar{f}$ is the same for all the control points. In this appendix, we provide an alternative formulation, which minimizes the maximum relative errors between the actual and prescribed force-displacement curves. The alternative formulation is stated as

$$
\begin{aligned}
\min_{\boldsymbol{\rho},\boldsymbol{\xi}} \ & \left\{ \max_{d_i} \left(\frac{f(d_i) - f^*(d_i)}{f^*(d_i)} \right)^2 + \theta \frac{\boldsymbol{v}^T \bar{\boldsymbol{\rho}}}{\bar{v}} \right\}, \quad i = 1, ..., n \\
\text{s.t.} \quad & \boldsymbol{r}\left(\bar{\boldsymbol{\rho}}, \bar{\boldsymbol{\xi}}, \boldsymbol{u}^i \right) = \boldsymbol{0}, \quad i = 1, ..., n \\
& \boldsymbol{v}^T \bar{\boldsymbol{\rho}} \le \bar{v} \\
& \left\{ \sum_{e=1}^{N} \left[\frac{\frac{1}{v_e} \int_{\Omega_e} \sigma^{VM}\left(\boldsymbol{\sigma}\left(\bar{\rho}_e, \bar{\xi}_e, \gamma_e, \boldsymbol{u}_e^n\right)\right) \mathrm{d}\boldsymbol{x}}{\bar{\sigma}\left(\bar{\rho}_e, \bar{\xi}_e\right)} \right]^p \right\}^{\frac{1}{p}} \le 1 \\
& \boldsymbol{0} \le \boldsymbol{\rho} \le \boldsymbol{1} \\
& \boldsymbol{0} \le \boldsymbol{\xi} \le \boldsymbol{1}.
\end{aligned}
\tag{A.1}
$$

In particular, the difference of the above formulation from (15) is in the normalization factor $f^*(d_i)$ in the objective function. The alternative formulation (A.1) normalizes the force error at control point d_i by the corresponding prescribed force $f^*(d_i)$. Depending on different design purposes, one can choose the alternative

relative error formulation (A.1) that emphasizes on the errors of the overall curve, or the proposed absolute error formulation (15) that tends to stresses on the points with larger force magnitudes.

We present two examples based on the alternative formulation (A.1). The two examples use the materials in Figure 3 **c** and prescribed Curve B in Figure 3 **f**. The first example uses a 150mm × 100mm domain with the "single cross" initial guess (Figure 3 **i**), and the second uses a 100mm × 100mm domain with the "double cross" initial guess (Figure 3 **j**). Other settings are the same as the previous examples.
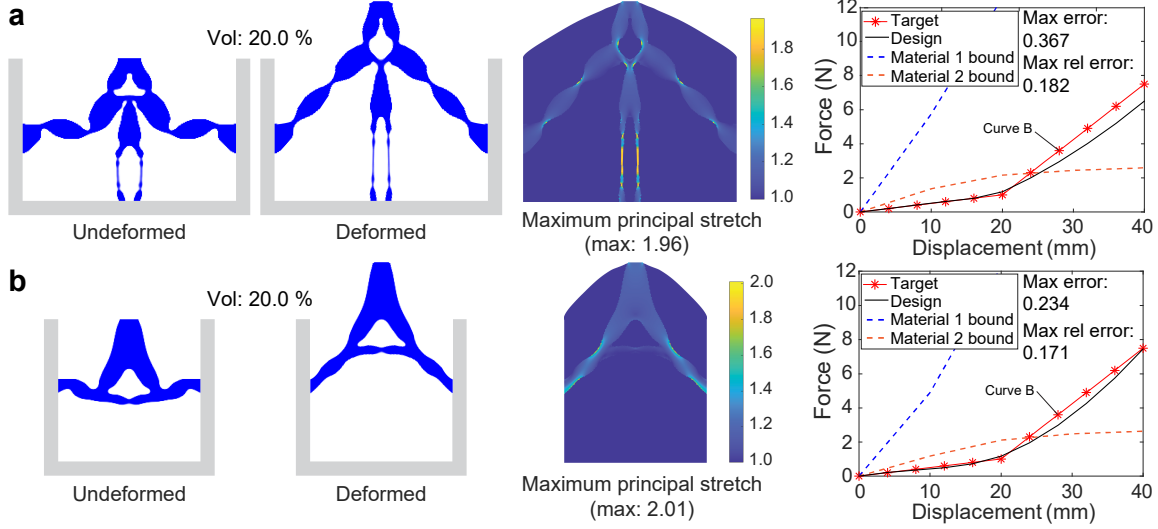

Figure A.10: Examples using alternative formulation (A.1). Designs, maximum principal stretches, and fittings of force-displacement curves of (a) 1.5:1 domain; and (b) 1:1 domain.

Table A.1: Comparison of fitting errors from the proposed and alternative formulation

Design	Normalized max absolute error (N)	Max relative error
Figure 6 **b** (formulation (15))	**0.087**	0.603
Figure A.10 **a** (formulation (A.1))	0.367	**0.182**
Figure 7 **a** (formulation (15))	**0.123**	0.775
Figure A.10 **b** (formulation (A.1))	0.234	**0.171**

Figure A.10 shows the designs, deformation, and fittings of the two optimized structures using the alternative formulation. The design in Figure A.10 **a** is obtained considering the same design parameters and target curve as the one shown in Figure 6 **b**, but with a different initial guess and formulation. Thus, different from the design in Figure 6 **b**, the optimized topology forms two branches attached to the side supports and two thin members connected to the bottom. The design in Figure A.10 **b** uses identical parameters and initial guess but different formulation compared with the one in Figure 7 **a**, which has a different topology. Both designs obtained using the alternative relative error formulation are governed by the underlying mechanism of changing deformation mode from flexure-dominated to stretch dominated, which is similar to the ones obtained by the proposed absolute error formulation (15) in Figures 6 **b** and 7 **a**. The mechanism is realized through the multiple hinges across the structures where deformation concentrates, leading to the acute increase in stiffness when loaded beyond 20 mm.

In terms of the fitting quality, the two designs obtained using the alternative relative error formulation achieve more accurate fittings in the first phase (displacement < 20 mm) but less accurate fitting in the

hardening phase, compared to the designs obtained using the proposed absolute error formulation in Figure 6 **b** and 7 **a**. The alternative formulation minimizes the relative error rather than the absolute one, putting more weight on minimizing the errors in the overall curve. In the absolute error formulation (15), the hardening phase with points of larger force magnitudes tend to have larger absolute errors, and thus, tends to have more weight. The two measurements of fitting errors for the four designs are shown in Table A.1, with the normalized maximum absolute error defined as $\max_{d_i}\left[f(d_i) - f^*(d_i)\right]/\bar{f}$ and maximum relative error defined as $\max_{d_i}\left[f(d_i) - f^*(d_i)\right]/f^*(d_i)$, the same quantities used in the objective functions of (15) and (A.1), respectively. As expected, the alternative relative error formulation (A.1) leads to designs with smaller maximum relative errors but larger normalized maximum absolute errors than the original proposed absolute error formulation (15).

Appendix B. Numerical verification of energy interpolation scheme

The energy interpolation scheme (9), which effectively alleviates numerical instabilities induced by low stiffness elements, has been demonstrated to have negligible influence on the performance of final optimized single-material designs in [25]. Appendix B further verifies the interpolation scheme on a multi-material design. We compare the force-displacement curve of the multi-material optimized structure in Figure 5, which includes the void regions in the FE analysis, with the force-displacement curve of the same design but with the void region entirely removed in the FE analysis. The comparison in Figure B.11 shows that the two force-displacement curves coincide and the deformed configurations are identical. Thus, the comparison verifies the modeling of the void region in the interpolation scheme (9) does not influence the behavior of the optimized structure under large deformations.
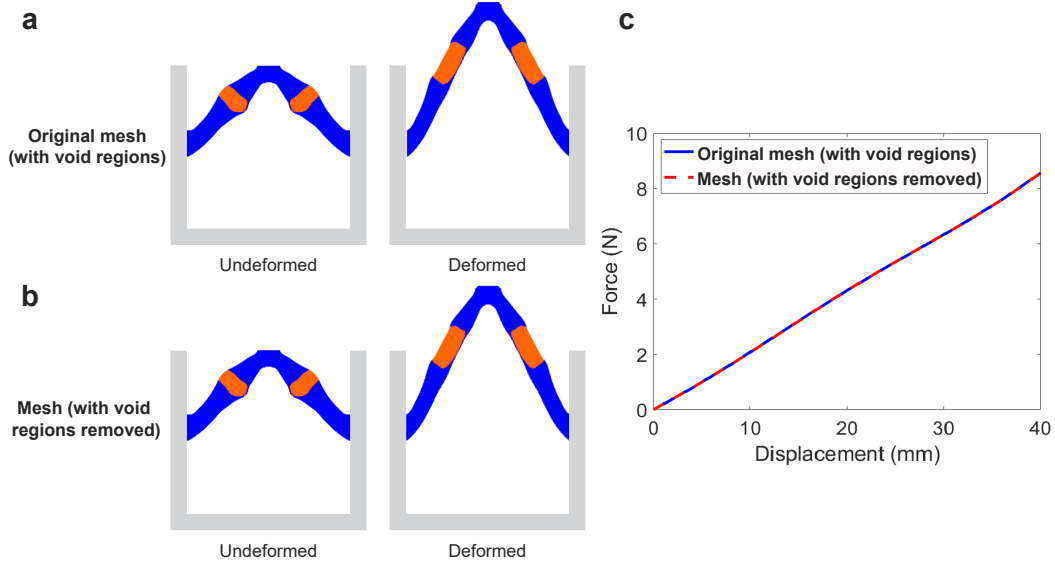

Figure B.11: Comparison of the structural responses of (a) a multi-material optimized design with the energy interpolation scheme in Eq. (9) and, (b) the same optimized design but with void elements entirely removed. (c) The corresponding force-displacement curves.

Appendix C. Effectiveness of the proposed two-material stress constraint

This appendix demonstrates that the proposed stress constraint for multi-material structures effectively eliminates thin members and unrealistically large deformation. We use the material models from Scenario 1

and a linear target curve, and compare the optimized designs obtained with and without the proposed stress constraint. Figure C.12 shows the two optimized designs, deformations, and fitting of target curves. It can be seen that in the design without stress constraint (Figure C.12 **a**), extremely thin members appear in the soft material regions, which leads to excessive deformation in the deformed configuration with a maximum principal stretch of 10.32. In contrast, the design with the proposed stress constraint (Figure C.12 **b**) contains no thin members, and the maximum stretch is 5.14. While both designs have good fit to the target curve, the extreme deformation in the non-constrained design should be difficult to realize with most types of elastomers. The comparison shows that the proposed stress constraint with von Mises stress measures effectively prevents thin members and extreme deformations in two-material structures.
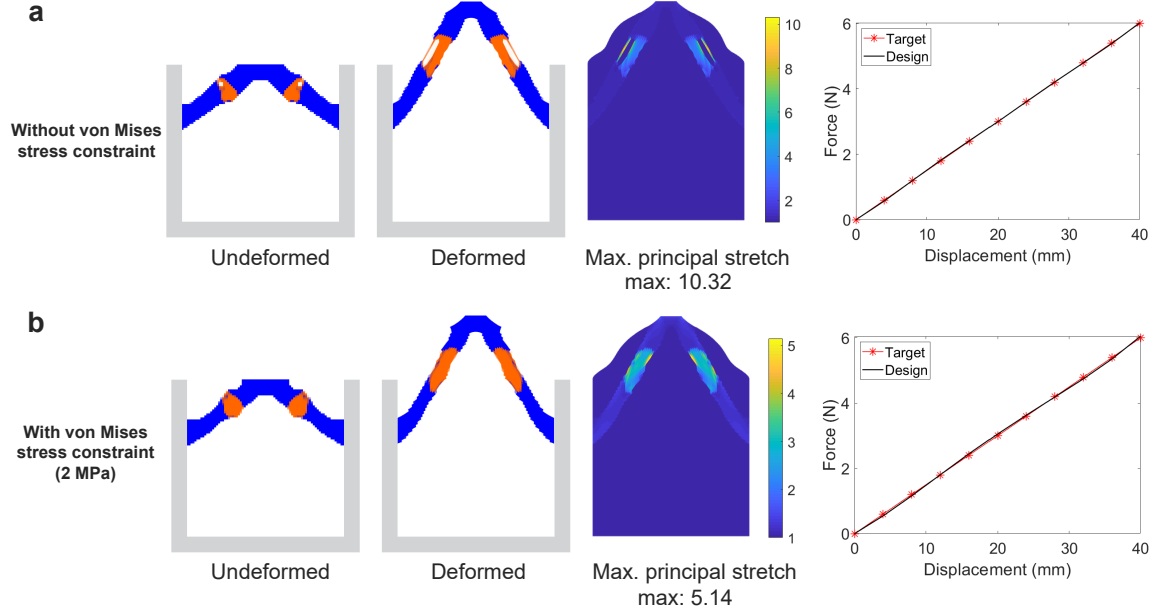

Figure C.12: Comparison of designs, deformations, and fitted curves obtained (a) without the proposed stress constraint and, (b) with the proposed stress constraint (2 MPa von Mises stress limit)

Appendix D. Discreteness of optimized designs

We provide quantitative measures for the discreteness of all optimized structures presented in Scenarios 1-3 to demonstrate the discreteness of both the density variable $\bar{\rho}_e$ and material variable $\bar{\xi}_e$, indicating solid-void designs with two spatially exclusive materials. The measure for discreteness of $\bar{\rho}_e$ and $\bar{\xi}_e$ are defined as [46] :

$$M_\rho = \frac{1}{N} \sum_{e=1}^{N} 4\bar{\rho}_e \left(1 - \bar{\rho}_e\right) \times 100\% \qquad \text{and} \qquad M_\xi = \frac{1}{N_S} \sum_{e \in S} 4\bar{\xi}_e \left(1 - \bar{\xi}_e\right) \times 100\%,$$

respectively, where S is the element set with $\bar{\rho}_e > 0$, and N_S is the number of elements belong to S. Measurement $M_\rho = 1$ when $\bar{\rho}_e = 0.5 \,\forall\, e$, indicating a fully gray design, and $M_\rho = 0$ when $\bar{\rho}_e \in \{0,1\} \,\forall\, e$, indicating a fully discrete, solid-void design. Similarly, $M_\xi = 1$ when $\bar{\xi}_e = 0.5 \,\forall\, e \in S$, indicating a design with evenly-mixed materials, and $M_\xi = 0$ when $\bar{\xi}_e \in \{0,1\} \,\forall\, e \in S$, indicating two materials are fully separated. The values of M_ρ and M_ξ for all designs are summarized in Table D.2. Both $M_\rho < 1\%$ and $M_\xi < 1\%$ for all designs, which verify that the optimized designs are near-discrete with minimal mixing of phases.

Table D.2: Discreteness of optimized structures

Scenario #	Design	Figure	M_ρ	M_ξ
	Two-material	Figure 5	0.52 %	0.59 %
Scenario 1	Material 1	Figure 4 a	0.79 %	0
	Material 2	Figure 4 b	0.28 %	0
	Curve A	Figure 6 a	0.74 %	0.04 %
	Curve B	Figure 6 b	0.55 %	0.00 %
Scenario 2	Curve C	Figure 6 c	0.75 %	0.00 %
	Curve C, initial guess 2	Figure 7 a	0.71 %	0.00 %
	Curve C, initial guess 3	Figure 7 b	0.57 %	0.00 %
	Two-material	Figure 9	0.50 %	0.30 %
Scenario 3	Material 1	Figure 8 a	0.43 %	0
	Material 2	Figure 8 b	0.27 %	0

Acknowledgments

References

[1] F. Wang, O. Sigmund, J. Jensen, Design of materials with prescribed nonlinear properties, Journal of the Mechanics and Physics of Solids 69 (2014) 156 – 174. `doi:10.1016/j.jmps.2014.05.003`.

[2] F. Wang, Systematic design of 3D auxetic lattice materials with programmable poisson's ratio for finite strains, Journal of the Mechanics and Physics of Solids 114 (2018) 303 – 318. `doi:10.1016/j.jmps.2018.01.013`.

[3] K.-I. Jang, H. U. Chung, S. Xu, C. H. Lee, H. Luan, J. Jeong, H. Cheng, G.-T. Kim, S. Y. Han, J. W. Lee, J. Kim, M. Cho, F. Miao, Y. Yang, H. N. Jung, M. Flavin, H. Liu, G. W. Kong, K. J. Yu, S. I. Rhee, J. Chung, B. Kim, J. W. Kwak, M. H. Yun, J. Y. Kim, Y. M. Song, U. Paik, Y. Zhang, Y. Huang, J. A. Rogers, Soft network composite materials with deterministic and bio-inspired designs, Nature Communications 6 (1) (2015) 6566. `doi:10.1038/ncomms7566`.

[4] A. Rafsanjani, A. Akbarzadeh, D. Pasini, Snapping mechanical metamaterials under tension, Advanced Materials 27 (39) (2015) 5931–5935. `doi:10.1002/adma.201502809`.

[5] S. Shan, S. H. Kang, J. R. Raney, P. Wang, L. Fang, F. Candido, J. A. Lewis, K. Bertoldi, Multistable architected materials for trapping elastic strain energy, Advanced Materials 27 (29) (2015) 4296–4301. `doi:10.1002/adma.201501708`.

[6] K. Fu, Z. Zhao, L. Jin, Programmable granular metamaterials for reusable energy absorption, Advanced Functional Materials 29 (32) (2019) 1901258. `doi:10.1002/adfm.201901258`.

[7] O. Sigmund, Materials with prescribed constitutive parameters: An inverse homogenization problem, International Journal of Solids and Structures 31 (17) (1994) 2313 – 2329. `doi:10.1016/0020-7683(94)90154-6`.

[8] O. Sigmund, Tailoring materials with prescribed elastic properties, Mechanics of Materials 20 (4) (1995) 351 – 368. `doi:10.1016/0167-6636(94)00069-7`.

[9] L. H. Dudte, E. Vouga, T. Tachi, L. Mahadevan, Programming curvature using origami tessellations, Nature Materials 15 (5) (2016) 583–588. `doi:10.1038/nmat4540`.

[10] A. Russomanno, Z. Xu, S. O'Modhrain, B. Gillespie, A pneu shape display: Physical buttons with programmable touch response, in: 2017 IEEE World Haptics Conference (WHC), 2017, pp. 641–646. `doi:10.1109/WHC.2017.7989976`.

[11] L. Wang, Y. Li, B. Chen, S. Liu, M. Li, L. Zheng, P. Wang, T. J. Lu, F. Xu, Patterning cellular alignment through stretching hydrogels with programmable strain gradients, ACS Applied Materials & Interfaces 7 (27) (2015) 15088–15097, pMID: 26079936. `doi:10.1021/acsami.5b04450`.

[12] B. Gorissen, D. Melancon, N. Vasios, M. Torbati, K. Bertoldi, Inflatable soft jumper inspired by shell snapping, Science Robotics 5 (42). `doi:10.1126/scirobotics.abb1967`.

[13] J. T. B. Overvelde, T. Kloek, J. J. A. D'haen, K. Bertoldi, Amplifying the response of soft actuators by harnessing snap-through instabilities, Proceedings of the National Academy of Sciences 112 (35) (2015) 10863–10868. `doi:10.1073/pnas.1504947112`.

[14] O. Sigmund, S. Torquato, Design of materials with extreme thermal expansion using a three-phase topology optimization method, Journal of the Mechanics and Physics of Solids 45 (6) (1997) 1037 – 1067. `doi:10.1016/S0022-5096(96)00114-7`.

[15] R. T. Bonnecaze, G. J. Rodin, O. Sigmund, J. Søndergaard Jensen, Systematic design of phononic band-gap materials and structures by topology optimization, Philosophical Transactions of the Royal Society of London. Series A: Mathematical, Physical and Engineering Sciences 361 (1806) (2003) 1001–1019. `doi:10.1098/rsta.2003.1177`.

[16] D. C. Dobson, S. J. Cox, Maximizing band gaps in two-dimensional photonic crystals, SIAM Journal on Applied Mathematics 59 (6) (1999) 2108–2120. `doi:10.1137/S0036139998338455`.

[17] O. Sigmund, S. Torquato, I. A. Aksay, On the design of 1–3 piezocomposites using topology optimization, Journal of Materials Research 13 (4) (1998) 1038–1048. `doi:10.1557/JMR.1998.0145`.

[18] T. Bruns, O. Sigmund, Toward the topology design of mechanisms that exhibit snap-through behavior, Computer Methods in Applied Mechanics and Engineering 193 (36) (2004) 3973 – 4000. `doi:10.1016/j.cma.2004.02.017`.

[19] J. Lee, T. Detroux, G. Kerschen, Enforcing a force–displacement curve of a nonlinear structure using topology optimization with slope constraints, Applied Sciences 10 (2020) 2676. `doi:10.3390/app10082676`.

[20] G. A. da Silva, A. T. Beck, O. Sigmund, Topology optimization of compliant mechanisms considering stress constraints, manufacturing uncertainty and geometric nonlinearity, Computer Methods in Applied Mechanics and Engineering 365 (2020) 112972. `doi:10.1016/j.cma.2020.112972`.

[21] A. Bandyopadhyay, B. Heer, Additive manufacturing of multi-material structures, Materials Science and Engineering: R: Reports 129 (2018) 1 – 16. `doi:10.1016/j.mser.2018.04.001`.

[22] X. S. Zhang, G. H. Paulino, A. S. Ramos, Multi-material topology optimization with multiple volume constraints: a general approach applied to ground structures with material nonlinearity, Structural and Multidisciplinary Optimization 57 (1) (2018) 161–182. `doi:10.1007/s00158-017-1768-3`.

[23] A. Takezawa, M. Kobashi, Design methodology for porous composites with tunable thermal expansion produced by multi-material topology optimization and additive manufacturing, Composites Part B: Engineering 131 (2017) 21 – 29. `doi:10.1016/j.compositesb.2017.07.054`.

[24] G. Zhang, K. Khandelwal, Computational design of finite strain auxetic metamaterials via topology optimization and nonlinear homogenization, Computer Methods in Applied Mechanics and Engineering 356 (2019) 490 – 527. `doi:10.1016/j.cma.2019.07.027`.

[25] F. Wang, B. S. Lazarov, O. Sigmund, J. S. Jensen, Interpolation scheme for fictitious domain techniques and topology optimization of finite strain elastic problems, Computer Methods in Applied Mechanics and Engineering 276 (2014) 453 – 472. `doi:10.1016/j.cma.2014.03.021`.

[26] R. W. Ogden, Non-linear Elastic Deformation, Dover Publications, 1997.

[27] Z.-Q. Feng, F. Peyraut, Q.-C. He, Finite deformations of ogden's materials under impact loading, International Journal of Non-Linear Mechanics 41 (4) (2006) 575 – 585. `doi:10.1016/j.ijnonlinmec.2006.02.003`.

[28] O. Zienkiewicz, R. Taylor, D. Fox, The Finite Element Method for Solid and Structural Mechanics, 7th Edition, Butterworth-Heinemann, Oxford, 2014. `doi:10.1016/C2009-0-26332-X`.

[29] L. Armijo, Minimization of functions having lipschitz continuous first partial derivatives., Pacific Journal of Mathematics 16 (1966) 1–3. `doi:10.2140/pjm.1966.16.1`.

[30] X. Zhang, A. S. Ramos, G. H. Paulino, Material nonlinear topology optimization using the ground structure method with a discrete filtering scheme, Structural and Multidisciplinary Optimization 55 (6) (2017) 2045–2072. `doi:10.1007/s00158-016-1627-7`.

[31] M. P. Bendsøe, O. Sigmund, Topology Optimization: Theory, Methods and Applications, Springer, Berlin, Heidelberg, 2003. `doi:10.1007/978-3-662-05086-6`.

[32] M. P. Bendsøe, O. Sigmund, Material interpolation schemes in topology optimization, Archive of Applied Mechanics 69 (9) (1999) 635–654. `doi:10.1007/s004190050248`.

[33] O. Sigmund, Design of multiphysics actuators using topology optimization – part ii: Two-material structures, Computer Methods in Applied Mechanics and Engineering 190 (49) (2001) 6605 – 6627. `doi:10.1016/S0045-7825(01)00252-3`.

[34] F. Wang, B. S. Lazarov, O. Sigmund, On projection methods, convergence and robust formulations in topology optimization, Structural and Multidisciplinary Optimization 43 (6) (2011) 767–784. `doi:10.1007/s00158-010-0602-y`.

[35] X. S. Zhang, H. Chi, G. H. Paulino, Adaptive multi-material topology optimization with hyperelastic materials under large deformations: A virtual element approach, Computer Methods in Applied Mechanics and Engineering 370 (2020) 112976. `doi:10.1016/j.cma.2020.112976`.

[36] M. P. Bendsøe, Optimal shape design as a material distribution problem, Structural optimization 1 (4) (1989) 193–202. `doi:10.1007/BF01650949`.

[37] G. Cheng, X. Guo, ϵ-relaxed approach in structural topology optimization, Structural optimization 13 (4) (1997) 258–266. `doi:10.1007/BF01197454`.

[38] G. Cheng, Z. Jiang, Study on topology optimization with stress constraints, Engineering Optimization 20 (2) (1992) 129–148. `doi:10.1080/03052159208941276`.

[39] M. Bruggi, On an alternative approach to stress constraints relaxation in topology optimization, Structural and Multidisciplinary Optimization 36 (2) (2008) 125–141. `doi:10.1007/s00158-007-0203-6`.

[40] P. Duysinx, O. Sigmund, New developments in handling stress constraints in optimal material distribution, 7th AIAA/USAF/NASA/ISSMO Symposium on Multidisciplinary Analysis and Optimization, American Institute of Aeronautics and Astronautics, 1998, 0. `doi:10.2514/6.1998-4906`.

[41] T. E. Bruns, D. A. Tortorelli, Topology optimization of non-linear elastic structures and compliant mechanisms, Computer Methods in Applied Mechanics and Engineering 190 (26) (2001) 3443 – 3459. `doi:10.1016/S0045-7825(00)00278-4`.

[42] N. Olhoff, Multicriterion structural optimization via bound formulation and mathematical programming, Structural optimization 1 (1) (1989) 11–17. `doi:10.1007/BF01743805`.

[43] K. Svanberg, The method of moving asymptotes—a new method for structural optimization, International Journal for Numerical Methods in Engineering 24 (2) (1987) 359–373. `doi:10.1002/nme.1620240207`.

[44] X. Poulain, V. Lefèvre, O. Lopez-Pamies, K. Ravi-Chandar, Damage in elastomers: nucleation and growth of cavities, micro-cracks, and macro-cracks, International Journal of Fracture 205 (1) (2017) 1–21. `doi:10.1007/s10704-016-0176-9`.

[45] R. Ogden, Elastic deformations of rubberlike solids, in: H. HOPKINS, M. SEWELL (Eds.), Mechanics of Solids, Pergamon, Oxford, 1982, pp. 499 – 537. `doi:10.1016/B978-0-08-025443-2.50021-5`.

[46] O. Sigmund, Morphology-based black and white filters for topology optimization, Structural and Multidisciplinary Optimization 33 (4) (2007) 401–424. `doi:10.1007/s00158-006-0087-x`.